

Strong Lewis-acid coordinated PEO electrolyte achieves 4.8 V-class all-solid-state batteries over 580 Wh kg⁻¹

Received: 11 June 2024

Accepted: 30 September 2024

Published online: 23 October 2024

Check for updates

Hanwen An¹, Menglu Li¹, Qingsong Liu¹, Yajie Song¹, Jiaxuan Liu¹, Zhihang Yu², Xingjiang Liu²✉, Biao Deng³ & Jiajun Wang^{1,2,4,5}✉

Polyethylene oxide (PEO) based electrolytes critically govern the security and energy density of solid-state batteries, but typically suffer from poor oxidation resistance at high voltages, which limits the energy density of batteries. Here, we report a Lewis-acid coordinated strategy to significantly improve the cyclic stability of 4.8 V-class PEO-based battery. The introduced Mg²⁺ and Al³⁺ with strong electron-withdrawing capability weaken the electron density of ether oxygen (EO) chains via chelation in the coordination structure, resulting in a locally limited interaction between the EO chains and the surface of cathodes at high state of charge. The batteries using Lewis-acid coordinated electrolytes and Ni-rich cathodes achieve high voltage stability of 4.8 V over 300 cycles. Further, the realization of industrial-scale electrolyte membranes, and Ah-level pouch cells over 586 Wh kg⁻¹ with good cyclic stability, suggests the potential of our strategy in practical applications of all-solid-state batteries.

All-solid-state Li metal batteries (ASSLBs) using polymer as electrolyte are widely recognized as the most promising system to achieve high energy density and improved security^{1–6}. Polyethylene oxide (PEO)-based solid polymer electrolytes show great potential to realize this goal for easy processability and good physical contact^{7–9}, but suffer from poor oxidation stability at high voltages^{10–14}. The notorious interfacial adaptability between the state-of-the-art layered Ni-Rich materials and PEO-based electrolytes remains a critical challenge^{15–18}.

Tremendous efforts have been devoted to solving the interfacial problems of polymer electrolytes at high voltage. The chemical deterioration of PEO is generally acknowledged as the primary factor leading to battery failure¹⁹. Protective methods, including inorganic filler^{20,21}, cathode coating^{22–24}, and molecular grafting^{25,26} have been pursued to extend the working voltage windows of solid-state batteries. The 4.5 V-class PEO-based solid-state batteries have been successfully developed²⁶. However, the inherent low oxidative potential of ether oxygen (EO) chains impedes their applications in ultra-high

voltage solid-state batteries (for example, 4.8 V-class ASSLBs)^{27–29}. It is urgently necessary to explore the failure mechanism within the voltage range of 4.5–4.8 V and create new design of electrolytes.

Recently, the high-concentration salt concept has proved to be effective in improving the high-voltage resistant ability of electrolytes^{30,31}, as the highly reactive EO chains and anions are involved in the more stable coordination structure³². Despite this strategy providing insight into tuning the coordination environment to overcome the poor stability, the ultralow ionic conductivity makes electrolytes unsuitable for Li⁺ migration during battery charging/discharging^{33,34}. Further, the metal ions-coordinated polymer was innovatively proposed to realize rapid Li⁺ conduction by chelating matrix molecules and expanding ion channels³⁵ but still challenged by the incompatibility of electrolytes with high-voltage cathodes³⁵. Inspired by the above coordination effect, it is hopeful that the tradeoff between oxidative stability and ionic conductivity can be decoupled by regulating the coordination mode in electrolytes.

¹MOE Engineering Research Center for Electrochemical Energy Storage and Carbon Neutrality in Cold Regions, School of Chemistry and Chemical Engineering, Harbin Institute of Technology, Harbin, PR China. ²National Key Laboratory of Chemical and Physical Power Sources, Tianjin Institute of Power Sources, Tianjin, PR China. ³Shanghai Institute of Applied Physics, Chinese Academy of Sciences, 239 Zhangheng Road, Shanghai, PR China. ⁴Harbin Institute of Technology, School of Chemistry and Chemical Engineering, Harbin, PR China. ⁵Chongqing Research Institute of HIT, Chongqing, PR China.

✉ e-mail: xjliu@nklps.org; jjjunhit@hit.edu.cn

Here we demonstrate a Lewis-acid coordinated PEO-based electrolyte to achieve high-energy 4.8 V-class batteries. The strongly electronegative EO chains are captured by introducing Mg^{2+} and Al^{3+} with strong electron-withdrawing capability to weaken its solvating ability for high valence Ni at high voltage³⁶. This effect decreased the strong reactivity between the EO group and $\text{LiNi}_{0.83}\text{Co}_{0.12}\text{Mn}_{0.05}\text{O}_2$ (Ni83) cathodes, which significantly improved the interface compatibility at 4.8 V³⁷. Besides, the typical coordination structure involved by Mg^{2+} and Al^{3+} and more anions shows low energy of the highest occupied molecular orbital (HOMO) and simultaneously forms an inorganic-enriched interphase³⁸. As a consequence, the Mg^{2+} and Al^{3+} -coordinated electrolytes (PEO-Mg-Al-LiTFSI) integrate high electrochemical oxidation potential (>5 V) with good ionic conductivity (0.23 mS cm^{-1} at room temperature). With the modified electrolyte, the 4.8 V-class all-solid-state batteries achieve 300 cycles. The pouch cells with the energy density of over 586 Wh kg^{-1} exhibit good cycling stability. The industrial-scale manufacture of electrolyte membranes demonstrates the great engineering application potential of this strategy.

Results

Ni-poor layers induced by strong solvating ability of PEO at high-voltage

To design high-voltage stable electrolytes against Ni-Rich layered cathodes, understanding the failure mechanism between PEO-based

electrolytes and cathodes is desirable. Especially charging over 4.3 V, which significantly improves the energy density, but needs a deep understanding of interface failure mechanism. Operando synchrotron transmission X-ray microscopy (TXM) was conducted to probe the correlation of PEO-cathode (Ni-rich) interface evolution with the voltage increase in solid-state batteries (Fig. 1a, b)^{39–42}. To conduct Operando TXM, an in-situ cell was constructed according to the design shown in Figs. S1–2 and installed it in the center of the sample stage.

In the range of 3.5–4.3 V, both PEO-based and liquid batteries show similar shape of charge curve, the discrepancy in voltage stage and capacity can be ascribed to sluggish migration of Li^+ in PEO electrolyte⁴³. Besides, as the outward direction along the radius (the point from No.1 to No.5) shown in Figs. S3, S4, the Ni intensity of each point keeps steady with the voltage increasing⁴⁴. This result demonstrates unchanged Ni content from the surface to the bulk of Ni-rich cathodes in both PEO-based and liquid batteries. Although it has been proven that PEO electrolytes will decompose on the Ni-Rich cathode over 4.2 V⁴⁵, the Ni content at the interface is not significantly affected by the decomposition during the first cycle.

In the range of 4.3–4.8 V, for the liquid batteries, the redox reaction that occurs along all directions follows the phase-transition mechanism of layered cathode particles^{41,42}, as depicted by the Operando chemical mapping (Fig. 1a) and Ni K-edge X-ray absorption

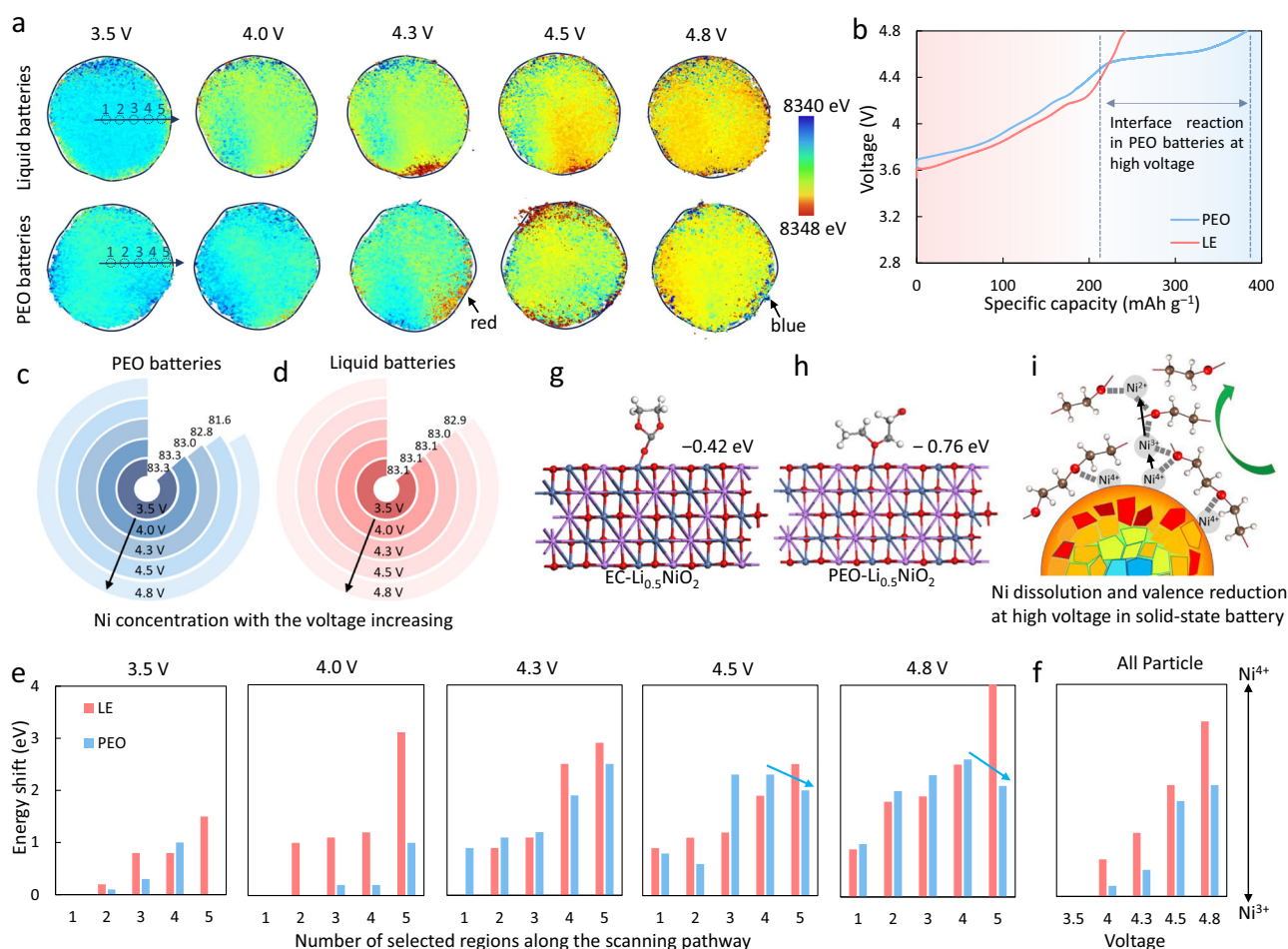


Fig. 1 | Strong interface interaction at high voltage. **a** Operando TXM mapping of cathode particles at different PEO and liquid voltages. **b** The charge curve of PEO batteries and liquid batteries. **c** The Ni concentration of Ni-Rich cathodes with different voltages in PEO batteries and **(d)** in liquid batteries. **e** Adsorption energy of EC and PEO **(f)** on the half-lithiated Li_xNiO_2 (104), gray, red, and purple balls

represent Ni, O, and Li atoms, respectively. **g** Energy shift at the near edge of Ni extracted from the XAS of each region at different voltages. **h** Energy shift of the whole particle in PEO and liquid batteries. **i** Schematic of the formation mechanism of the "Ni-poor" layer.

spectrums (XAS, Fig. S5a) from the surface to the bulk (No.1-No.5). However, for PEO batteries, there appears an extended voltage stage before reaching 4.5 V in the charging curve, the Ni concentration tested by inductively coupled plasma optical emission spectrometer (ICP-OES, Fig. 1c, d) and the peak intensity of the No.5 point extracted from Ni XAS (Fig. S5b) shows anomalous phenomenon of Ni content decrease on particle surface, indicating the formation of “Ni-poor” layer in this process. In addition, as the XAS extracted from the particle of 4.5 V shown in Fig. S4, the absorption edge shift of the surface (No.5) is less than that of the inner layer (No.4)⁴⁶, which demonstrates a lower valence state of Ni at the PEO-cathode interface. When the PEO batteries are last charged to 4.8 V, the Ni ratio on the surface decreases drastically and is accompanied by a more lower Ni valence state.

This “Ni-poor” effect at higher potentials (over 4.5 V) indicates that, in addition to the decomposition of PEO electrolytes, the PEO-cathode interface also exhibits a phenomenon of Ni dissolution on the surface of Ni-rich particles during the first charging. This is similar to the so-called “Ni dissolution” in liquid batteries after long cycling⁴⁷. Besides, the reduced absorption edge shift in the “Ni-poor” layer (Fig. 1e) demonstrates that, at high potential (4.5–4.8 V), high valence Ni is reduced to a low valence state during the oxidation of PEO, although the Ni valence of the whole cathode particle showed an increasing trend (Fig. 1f). The decrease of the Ni ratio can be explained by the strong interaction (−0.76 eV) between PEO and cathodes⁴⁸, while the adsorption energy of liquid electrolyte (Ethylene carbonate, EC) for high valent Ni is only −0.42 eV, as the adsorption energy calculated in the Fig. 1g, h. Under the strong adsorption of the EO chains, Ni migrates from the surface of the cathode to the electrolyte phase (Fig. 1i), resulting in interface degradation and battery failure. Therefore, high-voltage stable electrolytes against layered cathodes should satisfy both intrinsic high oxidation stability and, most importantly, weak interaction between EO chains and cathodes.

Lewis-acid coordinated strategy to weaken the solvating ability of electrolytes

Here we creatively introduce polyvalent cations as electron-withdrawing ligands for EO chains to control the interfacial interaction^{49–52}. The first criterion is ionic conductivity, electrolytes that only contain Al³⁺ have the highest ionic conductivity, followed by Mg²⁺ (Fig. S6a). High oxidation potential should be the second crucial requirement, electrolytes with Mg²⁺ alone show the highest oxidation stability window, followed by Al³⁺ (Fig. S6b). To improve the intrinsic oxidation-stability of electrolytes and weaken the interactions between cathodes and EO chains, Al³⁺ and Mg²⁺ (Fig. S6c, d) are simultaneously used to achieve complementarity and achieve their synergistic effects on ionic conductivity and voltage window. Additionally, the optimal molar ratio of Mg/Al: LiTFSI = 0.25 and M_w (2,000,000) of PEO was determined in electrolytes, which have the highest conductivity and improved oxidation potential (Figs. S7, S8). Therefore, the strong Lewis-acid additive of Mg(ClO₄)₂ and Al(ClO₄)₃ (EO: Li: Mg: Al = 18: 1: 0.25: 0.25) are employed to improve the intrinsic oxidation-stability of electrolytes and weaken the interactions between high valence Ni and EO chains^{53,54}.

Scanning electron microscope (Fig. S9) shows the homogeneous and dense structure. Karl-Fisher titration results demonstrate that perchlorates and electrolytes (165 ppm) have almost no water content after drying, which has almost no impact on battery performance⁵⁵ (Figs. S10–12). Thermogravimetric curve shows good thermal stability of the PEO-Mg-Al-LiTFSI electrolyte (Fig. S13).

The Mg²⁺ and Al³⁺ lead to a competitive coordination environment in electrolytes, the Li⁺ migration rates can be reinforced due to the weakened Li-O interactions and encapsulated TFSI[−]^{51,56,57} (Fig. 2a). Raman spectroscopy was employed to gain insights into electrolyte coordination behaviors (Fig. 2b). The band at 744 cm^{−1} is assigned to the ion pairs of TFSI[−] and the band at 740 cm^{−1} is assigned to the

dissociated TFSI[−]^{20,58}. The monotonic blue shift of these peaks demonstrates more TFSI[−] occupying the solvation sheath⁵⁹, which will reduce the migration number of anions. Additionally, the reduced peak intensity at 744 cm^{−1} suggests the facilitated dissociation of Li-TFSI ion pairs, indicating more free-Li⁺ for rapid ion transfer.

To gain further insight into the working mechanism of Lewis acid, molecular dynamics (MD) simulations were performed to reveal the coordination configurations of electrolytes. The molecular legend is depicted in Fig. S4d. As the snapshot of PEO-LiTFSI shown in Fig. 2c, the typical configuration displays that the Li⁺ form coordination with O atoms (EO chains) and TFSI[−]. The radial distribution functions (RDF) (Fig. 2d) show strong peaks of Li-EO chains and Li-TFSI coordination, and their high coordination numbers (CN), meaning the strong constraints on Li⁺. This result suggests that strong binding of Li-EO and Li-TFSI will cause concentration polarization in batteries⁶⁰. In comparison, benefitting from the electron-withdrawing effect of additives, the typical coordination configurations of PEO-Mg-Al-LiTFSI show that anions extensively enter the inner solvation sheath (Fig. 2e), which results in a preferential formation of an anion-derived cathode electrolyte interphase (CEI)⁶¹. Besides, the decreased peak intensity of Li-EO and Li-TFSI coordination and reduced coordination number indicate a faster Li⁺ diffusion. The increased distance (from 2.056 Å to 2.075 Å) between Li⁺ and EO in PEO-Mg-Al-LiTFSI also demonstrates the weakened interaction of the Li-EO bond, which corresponds to the RDF analysis³⁰. Finally, the Mg²⁺ and Al³⁺ show strong interaction with EO chains and TFSI[−] anions, as the RDF of Mg/Al/O/TFSI[−] calculated in Fig. 2f–h, compared to Li, Mg²⁺, and Al³⁺ have greater intensity peaks and coordination numbers when interacting with TFSI[−] and EO chains, which result in mostly coordinated EO chains and protect them from oxidation³².

Electrolyte performance for high-voltage cathodes

To investigate the oxidation resistance of the coordination structure, the electrostatic potential (ESP) distribution is explored to account for the local interaction at the electrolyte-cathode interface. As seen in Fig. 3a, the Lewis-acid coordinated EO chains show decreased electron density compared with Li-coordinated EO chains (PEO-LiTFSI), which manifests a weak interaction of PEO-Mg-Al-LiTFSI against the Ni-rich cathode at high state of charge⁶². Note that the enlarged region of negative area on the surface of the structure sheath indicates a preferential decomposition of inorganic anions, which is beneficial for forming high-voltage stable interphases⁶³. In addition, the Lewis-acid coordinated structure shows a low energy level (−9.08 eV) of the highest occupied molecular orbital (HOMO) (Fig. 3b), confirming its good oxidation resistance ability⁶¹.

It is important to note that differences in coordination structures can explain variations in the electrochemical performances of electrolytes. Consequently, the features of the coordination structure have a significant impact on the oxidation potential. Linear sweep voltammetry (LSV) tests were further conducted to evaluate the antioxidation stability of electrolytes. The decomposition current that corresponds to the decomposition potential of the PEO-LiTFSI electrolyte can be used as the threshold for determining the decomposition potential of PEO-Mg-Al-LiTFSI. The PEO-LiTFSI electrolyte exhibits a noticeable current rise over 4.2 V (vs Li⁺/Li), while the PEO-Mg-Al-LiTFSI electrolyte shows improved antioxidation ability up to 5.0 V (vs Li⁺/Li) (Fig. 3c). Additionally, benefitting from the Lewis acid-modified competitive coordination for EO chains, the dissociation energy of Li⁺ from the coordination structure drops from 0.75 eV to as low as 0.58 eV (Fig. 3d), which is considered as key for boosted Li ions transfer⁶⁴. Consequently, the dried (Table S2, Fig. S14) Lewis-acid coordinated electrolytes exhibit high ion conductivity of 0.23 mS cm^{−1} at room temperature (Fig. 3e). Indeed, it demonstrates superior ionic conductivity compared to PEO-LiTFSI electrolyte at temperatures below 60 °C.

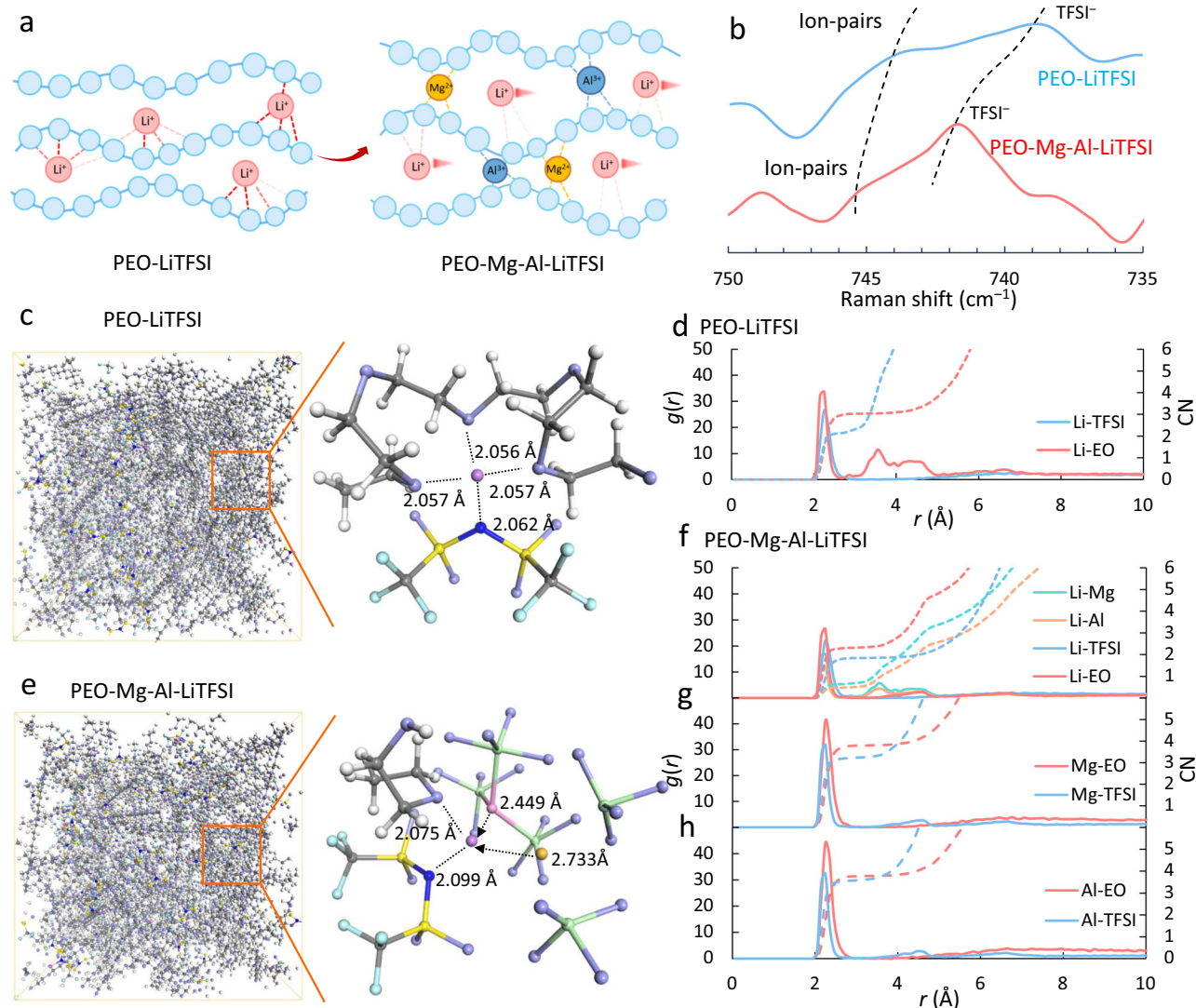


Fig. 2 | Regulating the coordination structure to weaken the interfacial interaction. **a** Schematic of the function of Lewis-acid additives. **b** Raman spectra of PEO-LiTFSI and PEO-Mg-Al-LiTFSI electrolytes. **c** Snapshots obtained from MD simulations of the PEO-LiTFSI electrolyte and **(d)** the corresponding radial

distribution functions. **e** Snapshots of the PEO-Mg-Al-LiTFSI electrolyte and **(f)** Radial distribution functions centered on the Li atom, **(g)** Mg atom, and **(h)** Al atom, white balls represent H atoms, as well as blue-N atoms, light purple-O atoms, yellow-S atoms, light blue-F atoms, pink-Al atoms, and orange-Mg atoms.

The ion diffusion coefficient, subsequently, was calculated to explore the transport properties of each ion in electrolytes⁶⁵. As shown in Fig. 3f, the Mg²⁺ and Al³⁺ in PEO-Mg-Al-LiTFSI are not mobile, as indicated by a negligible diffusion coefficient of $1.62 \times 10^{-10} \text{ cm}^2 \text{ s}^{-1}$ and $7.05 \times 10^{-11} \text{ cm}^2 \text{ s}^{-1}$, respectively. However, the Lewis-acid additives play an indispensable role in allowing fast Li⁺ transport, the PEO-LiTFSI displays a low Li⁺ conductivity ($4.80 \times 10^{-2} \text{ mS cm}^{-1}$) and diffusion coefficient ($1.21 \times 10^{-9} \text{ cm}^2 \text{ s}^{-1}$), by sharp contrast, the PEO-Mg-Al-LiTFSI displays a much higher diffusion coefficient of $5.30 \times 10^{-8} \text{ cm}^2 \text{ s}^{-1}$. Additionally, in PEO-Mg-Al-LiTFSI electrolyte, the diffusion coefficient ($5.3 \times 10^{-8} \text{ cm}^2 \text{ s}^{-1}$) of Li ions is 2.24 times the sum of the diffusion coefficients of TFSI⁻ ($1.9 \times 10^{-8} \text{ cm}^2 \text{ s}^{-1}$) and ClO₄⁻ ($4.6 \times 10^{-9} \text{ cm}^2 \text{ s}^{-1}$). And the higher coordination number (from RDF) of Mg-O (3.80) and Al-O (3.57) than Li-O (2.32) is also consistent with the diffusion analysis (Fig. 3g), resulting in the high transference number ($t_{\text{Li}^+} = 0.67$) in PEO-Mg-Al-LiTFSI (Fig. 3h). These results demonstrate the great practicality potential of PEO-Mg-Al-LiTFSI electrolytes in high loading composite cathodes.

For the compatibility between electrolyte and lithium anode, the Lowest Unoccupied Molecular Orbital (LUMO) calculations (Fig. S15) show that, compared to PEO electrolyte (-1.51 eV), the LUMO energy of PEO-Mg-Al-LiTFSI electrolyte (-2.11 eV) is slightly reduced. This is

characterized as an increase in anode interface impedance and cyclic overpotential (Figs. S16–17). The XPS analysis reveals that that in PEO-Mg-Al-LiTFSI batteries (Fig. S18), the anode solid electrolyte interphase (SEI) components may include organic compounds⁶⁶, carbonates, LiF, MgF₂, AlF₃, and Al₂O₃^{67,68}. These low conductivity components increase the interfacial impedance but may be beneficial for long-term cycling stability⁵¹.

The practicality of Lewis-acid coordinated electrolytes in high-energy batteries

To evaluate the capability of electrolytes that support higher voltages, we assembled all-solid-state Li lithium batteries (Fig. 4a, b), with PEO-Mg-Al-LiTFSI as cathode side electrolytes membrane and ion conductor in the composite cathode (Fig. S19). Note that the EO chains of Lewis-acid coordinated electrolytes show a rather small reaction energy of -0.42 eV on the half-lithiated Li_xNiO₂ (104), while the EO in PEO-LiTFSI is energetically favorable with a reaction energy of -1.48 eV (Fig. 4c, d), indicating good interface stability of Lewis-acid coordinated EO chains against the high voltage cathodes^{30,69}.

Figure 4e shows that the performance of full batteries with PEO-Mg-Al-LiTFSI as cathode side electrolytes (referred to below as PEO-

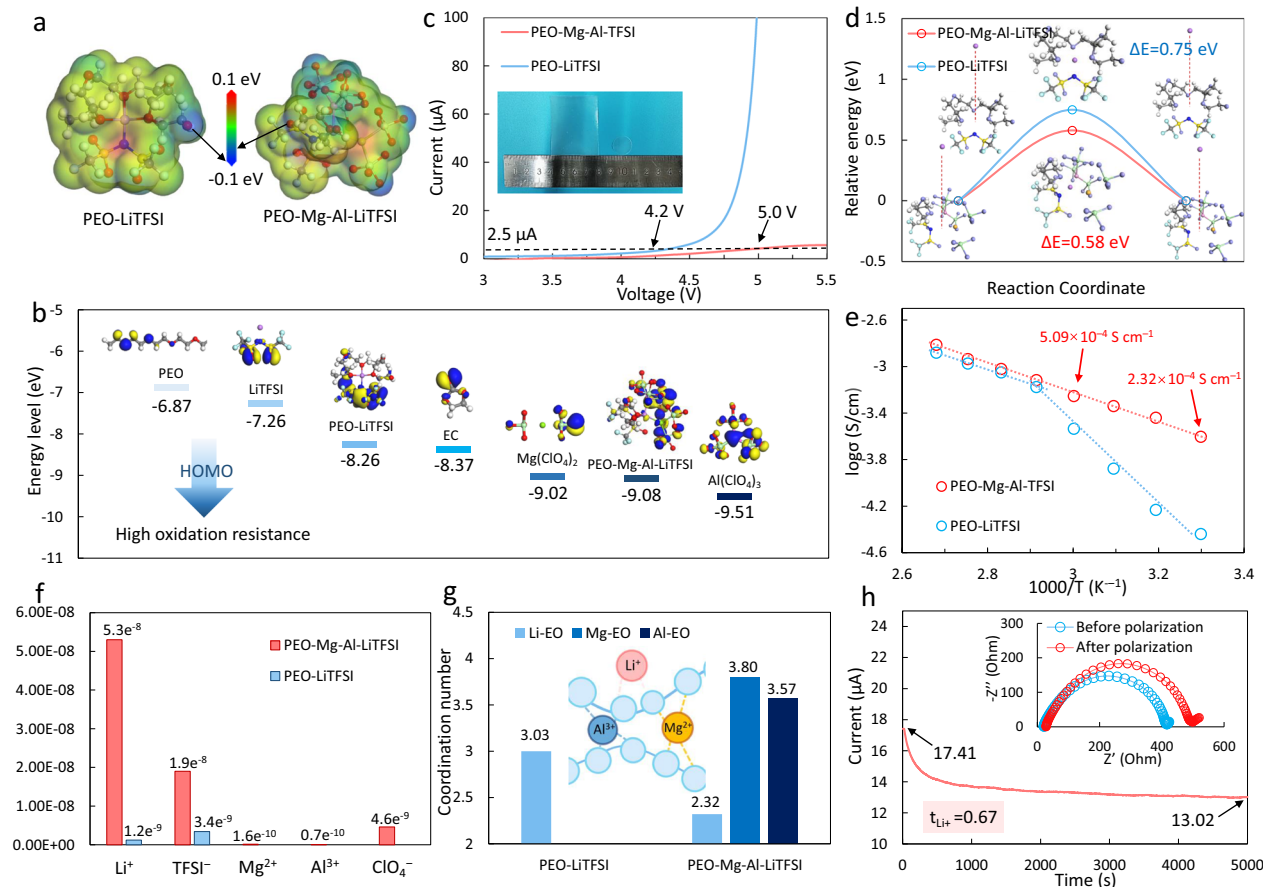


Fig. 3 | Electrolyte properties aiming at high voltage cathodes. a Electrostatic potential distribution of the typical coordination structure in PEO-LiTFSI and PEO-Mg-Al-LiTFSI electrolytes. **b** The HOMO energy values of each component. **c** Linear sweep voltammetry curve of PEO-LiTFSI and PEO-Mg-Al-LiTFSI electrolytes, with the threshold current of 2.5 μA . **d** The binding energy between Li and the typical coordination structure in PEO-LiTFSI and PEO-Mg-Al-LiTFSI electrolytes. **e** The ionic

conductivities of different electrolytes at different temperatures. **f** The ion diffusion coefficient of anions and cations in electrolytes. **g** Average Li-O, Mg-O, and Al-O coordination numbers from MD simulations of PEO-LiTFSI and PEO-Mg-Al-LiTFSI electrolytes. **h** Chronoamperometry curve for the PEO-Mg-Al-LiTFSI electrolyte with a polarization voltage of 10 mV and electrochemical impedance spectroscopy (EIS) plots before and after the polarization (inset).

Mg-Al-LiTFSI batteries) outperforms the PEO-LiTFSI batteries. Specifically, the PEO-Mg-Al-LiTFSI batteries exhibit a long cyclic performance over 300 cycles in the voltage range of 2.8–4.8 V. Even with a high loading of 15.1 mg cm^{-2} (Fig. S19a), it still delivers a high retention of 80.8% after 100 cycles. On the contrary, the PEO-LiTFSI batteries cannot charge and discharge at high cut-off voltage of 4.8 V. Electrochemical impedance spectroscopy (EIS) investigation of cycled batteries was conducted, as depicted in Fig. 4f, the PEO-Mg-Al-LiTFSI batteries show low interface impedance (R_{inter}) after 100 cycles while the PEO-LiTFSI batteries suffer from a sharp increase of R_{inter} after only 3 cycles. These results agree well with the density functional theory (DFT) calculations. The corresponding charge-discharge voltage profiles of the batteries at different cycles, as seen in Fig. 4g, demonstrate low electrochemical polarization in PEO-Mg-Al-LiTFSI batteries. On the contrary, the highly reactive interface severely degrades the capacity of PEO batteries (Fig. S20a)¹⁷.

To better represent practical conditions, the PEO-Mg-Al-LiTFSI pouch cells were evaluated and delivered a discharge energy density of 586 Wh kg^{-1} (bare cell = 645 Wh kg^{-1} , Fig. 4h) at 0.1 C. More importantly, high retention of capacity (80.6%) is observed even after 50 cycles (Fig. 4i, 100 cycles with retention of 63.5%). The high energy density of batteries indicates the ability of intelligent equipment to endure ultralong. Figure 4j shows the potential for uncrewed aerial vehicles expected to operate at much longer mileage. As shown in Figs. S20b–d, S21, we further assembled PEO-Mg-Al-LiTFSI batteries

and liquid batteries with Li-Rich $\text{Li}_{1.14}\text{Ni}_{0.136}\text{Co}_{0.136}\text{Mn}_{0.542}\text{O}_2$ materials as cathode, the batteries show a high retention of 74.7% after 100 cycles. While liquid batteries have a retention rate of 61.8% after 100 cycles, and they are incapable of operating at elevated temperatures. In addition, the battery's capacity retention using PEO-LiTFSI after 100 cycles, within the voltage range of 2.8–4.2 V, was found to be only 28.1%. Comparatively, the PEO-Mg-Al-LiTFSI batteries were evaluated for their cycle performance within the voltage range of 2.8–4.6 V and 2.8–4.7 V, as shown in Fig. S22. The improved stability of the high voltage batteries supports the fact that the “Lewis-acid coordinated electrolytes” have great potential to promote the energy density of PEO-based batteries significantly.

Furthermore, a roll of PEO-Mg-Al-LiTFSI electrolyte membranes with a length of 50 m, width of 0.3 m was prepared using an industrial-scale continuous slurry-casting production line (Fig. 5a, b)⁷⁰, by coating the electrolyte slurry on a polyethylene (PE) substrate film. This flexible and transparent electrolyte shows uniformity of thickness and high quality of surface (Fig. 5c, d). The solid cathodes can be manufactured using similar processes by replacing PE and electrolyte slurry with current collector and composite electrode slurry, respectively. In addition, a 20 Ah all-solid-state polymer battery was assembled by the electrolyte membrane obtained from the industrial-scale continuous process (Fig. 5e). The high capacity, high coulomb efficiency, and good cyclic performance of this device (Figs. S23–24) present the great potential of the Lewis-acid coordinated strategy in the engineering application.

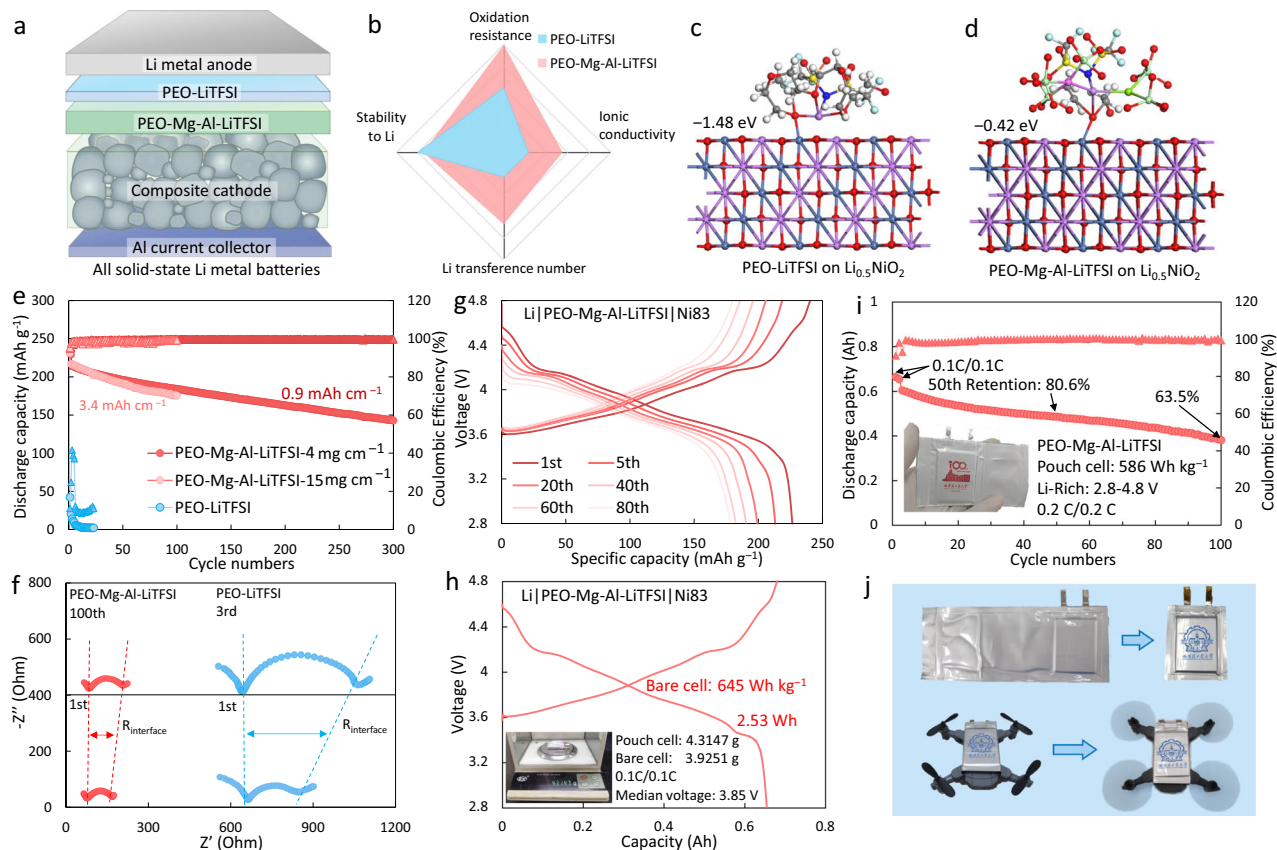


Fig. 4 | Batteries performance assembled by Lewis-acid coordinated electrolytes. **a** Schematic of the structure of PEO-Mg-Al-LiTFSI batteries. **b** Comparison chart of properties of electrolytes. **c** The adsorption energy of PEO-LiTFSI electrolyte on the half-lithiated Li_xNiO_2 . **d** Adsorption energy of PEO-Mg-Al-LiTFSI (EO- Li_xNiO_2) on the half-lithiated Li_xNiO_2 (104). **e** Cycling performance of PEO-LiTFSI

and PEO-Mg-Al-LiTFSI batteries. **f** EIS of PEO-LiTFSI and PEO-Mg-Al-LiTFSI batteries before and after cycling. **g** Galvanostatic charge/discharge voltage profiles of PEO-Mg-Al-LiTFSI. **h** Galvanostatic charge/discharge voltage profiles of pouch cells. **i** Cycling performance of PEO-Mg-Al-LiTFSI pouch cells. **j** Optical photos of PEO-Mg-Al-LiTFSI pouch cells and their application in micro drones.

Ultimately, we conducted the electrolyte moisture content (Table S3) under different dry environments with varying standing times, as well as the corresponding electrolyte impedance, the first Coulombic efficiency of the battery, and the impedance of lithium symmetric batteries. The PEO-Mg-Al-LiTFSI electrolyte exhibits stable ion conductivity, oxidation potential (Fig. S25), cathode interface stability (Fig. S26), and lithium metal interface stability (Fig. S27) in a moisture-free environment with standing time increasing, hence confirming its good chemical stability.

Investigation of the high voltage stable interface

Synchrotron TXM was further conducted to investigate the interaction between electrolyte and Ni-Rich cathode. As the 2D chemical phase mapped in Fig. 6a, the Ni83 particle (discharge state) in PEO-LiTFSI shows an enlarged area of local high SOC region after cycling⁴¹. In contrast, the cathode particle disassembled from PEO-Mg-Al-LiTFSI shows homogeneous SOC. The X-ray absorption spectrum (Fig. 6b) also presents that a clear shift of 1.5 eV occurs at the absorption edge of nickel in PEO-LiTFSI cathode particles, compared with PEO-Mg-Al-LiTFSI batteries⁴². This result indicates an improved interface stability benefited by the Lewis-acid coordinated effect, which promotes interfacial Li^+ transport and SOC homogeneity. Besides, the statistical intensity of nickel (Fig. 6c) and absorption edge shift (Figs. 6d, S28) shows that the content and valence of Ni element are consistent with the phase-transition mechanism in liquid batteries⁴³, manifesting a locally inhibited interaction between EO chains and cathode.

Synchrotron X-ray nano-tomography, subsequently, was used to explore the interphase structure after cycles. As reconstructed in Fig. 6e, a large area of X-ray weakly absorbed substance on the PEO-LiTFSI cathode surface can be assigned as organic components, while the surface of the PEO-Mg-Al-LiTFSI cathode particle shows a larger area of strong X-ray absorbent substance that corresponds to inorganic components⁴⁵. The quantitative analysis (Fig. 6f) also demonstrates an inorganic-dominant interphase of the PEO-Mg-Al-LiTFSI particle, which can inhibit continuous electrolyte oxidation and provide excellent interfacial stability⁷¹. These results also agree well with the DFT calculations of ESP and reaction energy. Besides, the higher porosity of PEO-LiTFSI particles (Fig. 6g) after cycles indicates more micro-cracks due to the severe surface degradation, which impedes ion transport in solid-state batteries⁷². By comparison, the PEO-Mg-Al-LiTFSI particle keeps low porosity, demonstrating structural integrity thanks to the uniform and stable CEI.

Interfacial chemistry was further investigated by conducting X-ray photoelectron spectroscopy (XPS). The cathode powder sample is obtained by dissolving the disassembled cathode sheet in acetonitrile solvent with further filtering and drying. As seen in Fig. 6h, the apparent signals of LiF , MgF_2 , and AlF_3 were observed on the surface of the PEO-Mg-Al-LiTFSI cathode, while PEO-LiTFSI cathode showed weaker signals of LiF ^{66,73}. We know that inorganics-abundant (LiF , MgF_2 , and AlF_3) interphases which are dense and robust, can block electron leakage and give rise to a low interface resistance^{51,74,75}. Thus, good interface compatibility can be obtained to improve the high-voltage stability of electrolytes.

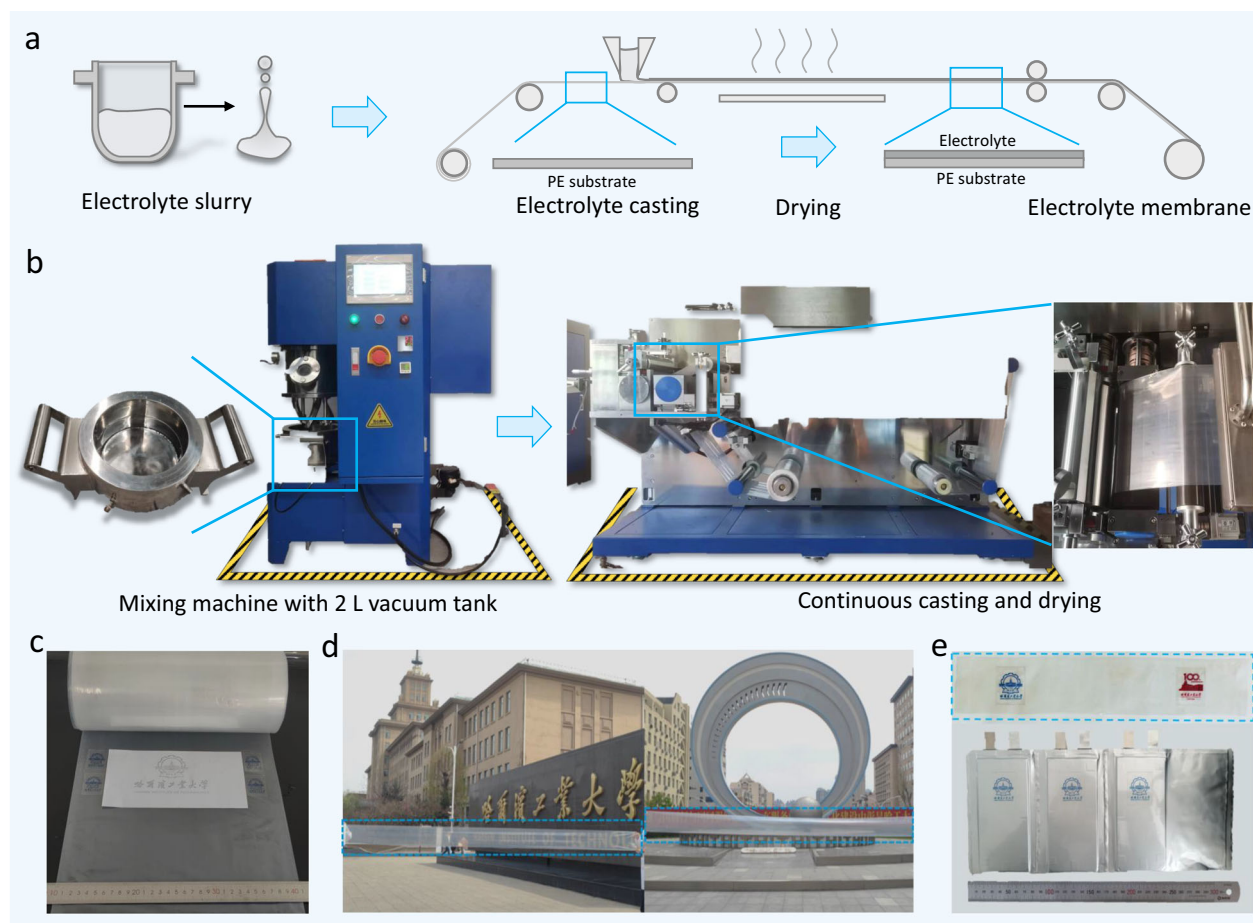


Fig. 5 | Industrial-scale membranes manufactured by continuous process. **a** Schematic of the manufacturing process of membranes. **b** Optical photos of industrial-scale continuous slurry-casting production line. **c, d** A roll of electrolyte

membranes with a length of 50 m, width of 0.3 m. **e** Optical photos of 20 Ah all-solid-state polymer battery.

Discussion

In summary, the strong interaction between EO chains and Ni-Rich cathode was diagnosed as a critical origin responsible for the failure of high voltage PEO-based batteries. Accordingly, Lewis-acid Mg^{2+} and Al^{3+} were introduced as electron-withdrawing ligands to control the solvation ability of EO chains and enhance the oxidation resistance of electrolytes. As a consequence, the Lewis-acid coordinated electrolytes demonstrate high electrochemical oxidation potential (>5 V) with good ionic conductivity (0.51 mS cm^{-1}). Further, the batteries with Lewis-acid coordinated electrolytes deliver good cyclic performance in the range of 2.8–4.8 V. A high energy density pouch cells over 586 Wh kg^{-1} (bare cell = 645 Wh kg^{-1}) achieved 100 cycles with a capacity retention of 63.5%. A roll of electrolyte membranes was prepared using an industrial-scale continuous process also shows the potential of a Lewis-acid coordinated strategy to significantly promote practical processes for high energy density ASSLBs.

Methods

Materials preparation

The PEO-LiTFSI electrolytes were prepared by a solution casting method and hot pressing at 80°C . 2.763 g Polyethylene oxide (PEO, $M_n = 2,000,000$, Aladdin, 99.9%) and 1 g lithium bis(trifluoromethane sulfonimide) (LiTFSI, Aladdin, 99%) were added into 100 g anhydrous acetonitrile (ACN, Aladdin, 99%) solutions, the EO:Li ratio is 18:1. After stirring for 12 h, the mixture of electrolyte solution was poured into a polytetrafluoroethylene mold and dried under vacuum at 60°C for 48 h. Finally, a solid-state electrolyte (PEO-LiTFSI) membrane was

obtained through hot pressing process. For PEO-Mg-Al-LiTFSI electrolytes, 5 g $Al(\text{ClO}_4)_3 \cdot 9\text{H}_2\text{O}$ (Aladdin, 99.9%) and 2.5 mg Al debris were mixed and heated 15 h at 150°C in the inert atmosphere (Ar) for dehydration, then the anhydrous $Al(\text{ClO}_4)_3$ was obtained. Next, 0.284 g anhydrous $Al(\text{ClO}_4)_3$, 0.194 g anhydrous $Mg(\text{ClO}_4)_2$, 1 g LiTFSI and 2.76 g PEO were added into 100 g anhydrous acetonitrile, stirring for another 12 h, then the obtained PEO-Mg-Al-LiTFSI electrolyte solution was poured into a polytetrafluoroethylene mold and dried under vacuum at 60°C for 48 h. Finally, PEO-Mg-Al-LiTFSI membrane was obtained through hot pressing process.

Preparation of high-voltage composite cathode and anode

$\text{LiNi}_{0.83}\text{Co}_{0.12}\text{Mn}_{0.05}\text{O}_2$ (Ni83) cathodes or Li-Rich $\text{Li}_{1.14}\text{Ni}_{0.136}\text{Co}_{0.136}\text{Mn}_{0.542}\text{O}_2$ materials, electrolyte (PEO-Mg-Al-LiTFSI electrolyte solution), and carbon nanotubes (CNTs) were added to N-Methyl pyrrolidone (NMP, Aladdin, 98%) solvent in a mass ratio of 85:12:3, and the uniform electrode slurry was obtained through a planetary agitator. Then the obtained slurry was coated on the aluminum current collector. Subsequently, the electrode is dried at 65°C for 24 h under vacuum to eliminate residual solvent. Finally, to prepare a dense composite cathode, press the dried cathode to 1 MPa cm^{-2} at 80°C . The pure lithium metal electrode used for assembling Coin-type batteries and the copper mesh-lithium metal composite foil used for assembling pouch cells were purchased from China Energy Lithium Co., Ltd.

Battery assembly: For PEO-Mg-Al-LiTFSI batteries, the CR2025 coin-type full batteries were assembled at a sealing pressure of 0.70 T

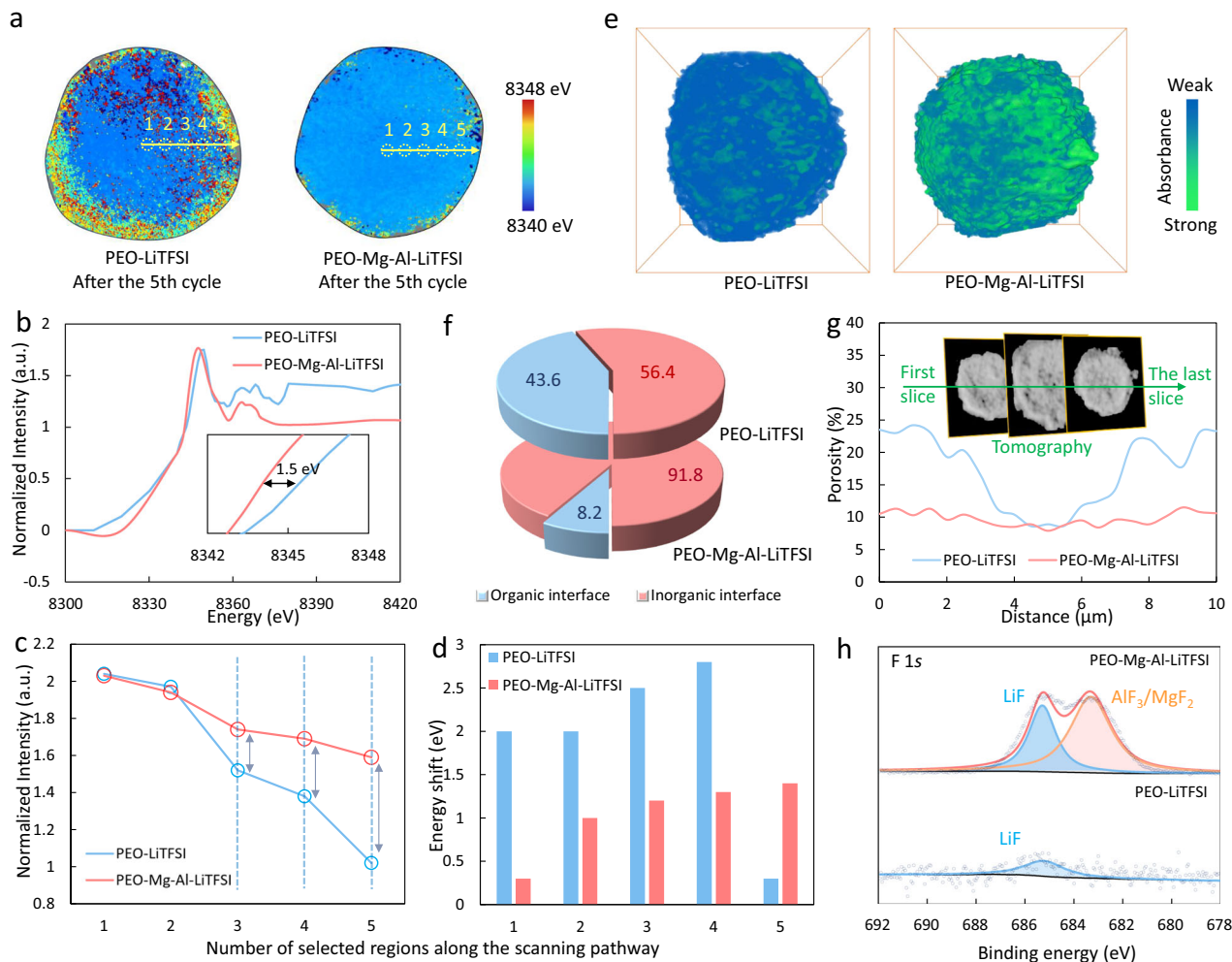


Fig. 6 | Interface investigation in high voltage batteries. **a** XTM mapping of the whole particle in PEO-LiTFSI and PEO-Mg-Al-LiTFSI batteries after 5 cycles. **b** The Ni XAS of the whole particle in PEO-LiTFSI and PEO-Mg-Al-LiTFSI batteries after 5 cycles. **c** The normalized Ni intensity of each region (No.1–No.5) in PEO-LiTFSI and PEO-Mg-Al-LiTFSI batteries. **d** Energy shift at the near edge of Ni extracted from the XAS of each region (No.1–No.5) at different voltages. **e** 3D structure of synchrotron

X-ray tomography for PEO-LiTFSI and PEO-Mg-Al-LiTFSI batteries after cycling, the viewpoint size of electrolyte is $10 \times 10 \times 10 \mu\text{m}^3$, green represents strong absorption of X-rays and blue represents weak absorption. **f** Quantitative analysis of inorganic area proportion. **g** The variation of porosity with distance of the Ni83 particle after cycling. **h** XPS spectra of F 1s of cycled Ni83 particle in PEO-LiTFSI and PEO-Mg-Al-LiTFSI batteries.

in glovebox filled with argon, where the lithium metal foil is used as the anode. The double layer electrolyte is used as the membrane. The PEO-LiTFSI ($\leq 15 \mu\text{m}$) is used as anode side membrane, PEO-Mg-Al-LiTFSI is used as cathode side membrane and ion conductor in cathode. Different composite cathodes as working cathodes, all the cathode with loading over 15 mg cm^{-2} . For pouch cells, Lithium copper (Copper mesh as current collector) composite foil is used as anode, the total thickness of anode is less than $20 \mu\text{m}$, the double layer electrolyte membrane is less than $40 \mu\text{m}$, the loading of cathode sets 50 mg cm^{-2} (double-sided coating), with the area of $32 \times 42 \text{ mm}^2$, made through hardware knife molds. Then four cathodes, five anodes and corresponding number of membranes were used to assemble an all-solid-state bare cell with 3.93 g . Next, polypropylene (PP) separator is used to wrap the bare cell to prevent short circuits. Aluminum-plastic film is used to encapsulate the battery (4.31 g) at the vacuum condition.

Electrochemical measurements

Galvanostatic charge/discharge measurements were performed on Neware battery test system (BTS-2004, Shenzhen, China) under 60°C , at atmospheric pressure, and the voltage ranges of batteries with Ni83 as cathode were adjusted to $2.8\text{--}4.8 \text{ V}$ ($1 \text{ C} = 200 \text{ mA g}^{-1}$), the batteries with Li-Rich as cathode were adjusted to $2.0\text{--}4.8 \text{ V}$ ($1 \text{ C} = 200 \text{ mA g}^{-1}$).

Pouch cells were tested under 1 MPa pressed by splint. The ionic conductivity of electrolyte films and all electrochemical impedance polymer electrolytes were evaluated by the electrochemical working station (Par-Solartron 663). The SS|PEO-LiTFSI|SS and SS|PEO-Mg-Al-LiTFSI|SS batteries were assembled with stainless steel sheet and electrolyte membrane. Ionic conductivity is calculated by the Eq. (1):

$$\sigma = \frac{L}{RS} \quad (1)$$

where L represents thickness of electrolyte membrane, the R resistance of battery, and S the contact area between steel sheet and electrolyte. The electrochemical window of the SPE was conducted by linear sweep voltammetry (LSV) technique in a battery that sandwiched the electrolyte between steel sheet and lithium metal at a sweep rate of 1 mV s^{-1} , 60°C . The lithium t_{Li^+} was calculated by Eq. (2):

$$t_{\text{Li}^+} = \frac{I_s \Delta V - I_0 R_0}{I_0 \Delta V - I_s R_s} \quad (2)$$

The initial current I_0 and the steady current I_s of a Li|SPE|Li cell were measured with a voltage pulse (ΔV) of 10 mV at the mode of DC

polarization. Electrochemical impedance spectroscopy was implemented before and after the DC polarization measurement to obtain the initial resistances R_0 and the final interfacial R_s . For the pouch cells test, a pressure mold is used for applying a pressure of 1 MPa on the battery. The screw can be adjusted using a torque wrench to ensure even distribution of force on the battery. The testing environment is atmospheric pressure and 60 °C. The activation conditions for all batteries are two cycles of charging and discharging at 0.1C.

Energy density calculation

According to the definition of battery energy density, it refers to the amount of energy (Wh) that a battery can release per unit mass (kg). Battery energy density (Wh kg⁻¹) = discharge energy (Wh)/battery quality (kg). The energy density of the pouch cell in this study was determined to be 586 Wh kg⁻¹ based on the discharge capacity acquired from the charge and discharge tester (2.53 Wh) and the battery mass measured using an electronic balance (4.32 g).

SEM, Raman, ICP-OES, TG

The morphology of cathode and powders was observed by field-emission scanning electron microscopy (SEM, Phenom Pro), and the smooth cross-section of the cathode was achieved by a cross-section ion polisher (accelerating voltage: 2–6 kV, beam spot size: 500 μm). Raman spectrum was recorded by Raman spectrometer (Renishaw). Inductively coupled plasma optical emission spectrometer (iCAP 7400) was used to test the element concentration of Ni-Rich cathodes disassembled from batteries at different voltages. The heating rate of the thermogravimetric (TG) curve is 5 °C for Al(ClO₄)₃ (keep 135 °C for 3 h) and 10 °C for electrolytes, respectively.

XPS

The battery was disassembled in a drying room and the cathode was dissolved again using acetonitrile solvent to remove the PEO-based electrolyte. The cycled cathode powder can be further obtained through filtration and drying for XPS testing. X-ray Photoelectron Spectroscopy (XPS, ESCALAB 250Xi) was employed to investigate the surface evolution.

Transmission X-ray microscopy (TXM), TXM mapping and corresponding data analysis

The CT image of TXM with synchrotron X-ray was recorded at Shanghai Synchrotron Radiation Facility (SSRF), beamline BL18B. For CT samples, due to the need for rotation of the sample stage, the cathode sheet is precisely cut and positioned inside a capillary glass tube, securely fastened at the midpoint of the sample stage, ensuring that the capillary is perfectly perpendicular to the sample stage. At above 15 keV, for -180 projections over an angular range of 180° with a field of view of 20 × 20 μm². The raw data obtained is tomographically aligned and reconstructed⁷⁶. The reconstructed cathode 3D data was further processed by the software package Avizo (Thermo Fisher Scientific, Waltham, Massachusetts, USA) for 3D visualization and quantized data analysis. The in-operando TXM mapping imaging was performed on the model coin cell during the initial charging (delithiation) process. To study the chemical state evolution, in the glove box, disassemble the coin-type battery. In order to prevent oxidation of the lithium metal and subsequent damage to the sample, it is recommended to introduce acetonitrile solvent between the electrolyte and lithium metal. This will effectively separate the lithium metal anode. Next, the cathode sheet is cut to an appropriate size and installed it on the sample stage, then a full XAS image series is collected at each charging stage (voltage) during the delithiation process. Each XAS image series was measured by scanning Ni absorption K-edge from 8280 to 8500 eV⁷². The recorded data were processed by an open-source software of TXM-Wizard.

Density functional theory (DFT) calculations

Vienna Ab-initio Simulation Package (VASP) code was used to carry out the density functional theory (DFT) calculations⁷⁷, and the model was established using Materials Studio software. The exchange-correlation was processed using the Perdew-Burke-Ernzerhof (PBE) functional within the generalized gradient approximation (GGA), and the expansion of the electronic eigenfunctions was described by applying the projector augmented-wave pseudopotential (PAW) with a kinetic energy cut-off of 500 eV^{78,79}. A Γ -centered 1 × 1 × 1 Monkhorst-Pack k-point sampled the Brillouin-zone integration. Until energy and force reached a tolerance of 1 × 10⁻⁵ eV and 0.03 eV/Å, respectively, all atomic positions were totally loosened. The long-range interactions were taken into consideration using the dispersion-adjusted DFT-D technique⁸⁰. During the process of establishing the model, an organic compound with 18 EO chains was used as the PEO substrate, this compound has a 1: 1: 0.25: 0.25 molar ratio to LiTFSI, Al(ClO₄)₃, and Mg(ClO₄)₂, and a box of 50 × 50 × 50 Å was constructed. The interatomic potential of components was derived from the Optimized pseudo potential for Liquid Simulations all-atom (OPLS-AA) force field⁸¹. For PEO the parameters are from Jorgensen's original paper, for TFSI⁻ are developed by Minhaeng Cho, and Al³⁺/Mg²⁺ are developed by Biswarup Pathak's job^{82,83}. As for the entire system, we refer to the previous work on electrolyte solution systems^{84–88}, and use VASP's machine learning force field. During the molecular dynamics (MD) simulation, we employed a timestep of 3000 for the time integration, and the systems were running with a temperature of 300 K in the NVT ensemble for 500 ps. Calculations for the determination of binding energy (E_b) for decomposition reactions on a four-layer slab model of LiNiO₂ (104) were performed³⁰. The binding energy (E_b) of a complex formed between two molecules, A and B, can be calculated using the following Eq. (3):

$$E_b = E_{\text{complex}} - (E_A + E_B) \quad (3)$$

Where E_{complex} is the total energy of the molecular complex of A and B. E_A and E_B are the total energies of isolated molecules A and B, respectively. The electrostatic potential (ESP) and lowest unoccupied molecular orbital (LUMO)-highest occupied molecular orbital (HOMO) energy were conducted with the Gaussian09 package⁶³ at the level of B3LYP functional level with 6–311++(d, p) basis sets⁸⁹.

Reporting summary

Further information on research design is available in the Nature Portfolio Reporting Summary linked to this article.

Data availability

The data that support the plots within this paper and other findings of this study are available from the corresponding author upon request. Source data are provided in this paper. Source data are provided with this paper.

References

1. Yang, C. et al. Copper-coordinated cellulose ion conductors for solid-state batteries. *Nature* **598**, 590–596 (2021).
2. Weiss, M. et al. From liquid- to solid-state batteries: ion transfer kinetics of heteroionic interfaces. *Electrochem. Energy Rev.* **3**, 221–238 (2020).
3. Wang, H., An, H., Shan, H., Zhao, L. & Wang, J. Research progress on interfaces of all-solid-state batteries. *Acta Phys. Chim. Sin.* **0**, 2007070 (2020). -2007070.
4. Zhang, X., Cheng, X. & Zhang, Q. Nanostructured energy materials for electrochemical energy conversion and storage: a review. *J. Energy Chem.* **25**, 967–984 (2016).
5. Chen, L.-H. et al. In situ polymerization of 1,3-dioxolane infiltrating 3D garnet framework with high ionic conductivity and excellent

- interfacial stability for integrated solid-state Li metal battery. *Rare Met.* **41**, 3694–3705 (2022).
6. Zhao, C.-X. et al. Analytical noncovalent electrochemistry for battery engineering. *Nat. Chem. Eng.* **1**, 251–260 (2024).
 7. Su, X. et al. Polyethylene oxide-based composite solid electrolytes for lithium batteries: current progress, low-temperature and high-voltage limitations, and prospects. *Electrochem. Energy Rev.* **7**, 2 (2024).
 8. Liu, Y.-N. et al. Poly(*m*-phenylene isophthalamide)-reinforced polyethylene oxide composite electrolyte with high mechanical strength and thermostability for all-solid-state lithium metal batteries. *Rare Met.* **41**, 3762–3773 (2022).
 9. Zhao, S. et al. Research progress on the solid electrolyte of solid-state sodium-ion batteries. *Electrochem. Energy Rev.* **7**, 3 (2024).
 10. Hou, W., Ou, Y. & Liu, K. Progress on high voltage PEO-based polymer solid electrolytes in lithium batteries. *Chem. Res. Chin. Univ.* **38**, 735–743 (2022).
 11. Zhang, W. et al. Single-phase local-high-concentration solid polymer electrolytes for lithium-metal batteries. *Nat. Energy* **9**, 386–400 (2024).
 12. An, H. et al. Coupling two-dimensional fillers with polymer chains in solid polymer electrolyte for room-temperature dendrite-free lithium-metal batteries. *Energy Storage Mater.* **43**, 358–364 (2021).
 13. Cao, C. et al. Emerging X-ray imaging technologies for energy materials. *Mater. Today* **34**, 132–147 (2020).
 14. Liang, J.-Y. et al. Engineering janus interfaces of ceramic electrolyte via distinct functional polymers for stable high-voltage Li-metal batteries. *J. Am. Chem. Soc.* **141**, 9165–9169 (2019).
 15. Yusim, Y. et al. Evaluation and improvement of the stability of poly(ethylene oxide)-based solid-state batteries with high-voltage cathodes. *Angew. Chem. Int. Ed.* **62**, 18311–18318 (2023).
 16. Zeng, X.-X. et al. Reshaping lithium plating/stripping behavior via bifunctional polymer electrolyte for room-temperature solid li metal batteries. *J. Am. Chem. Soc.* **138**, 15825–15828 (2016).
 17. Fu, C. et al. Capacity degradation mechanism and improvement actions for 4 V-class all-solid-state lithium-metal polymer batteries. *Chem. Eng. J.* **392**, 123665 (2020).
 18. Chen, J., Wu, J., Wang, X., Zhou, A. A. & Yang, Z. Research progress and application prospect of solid-state electrolytes in commercial lithium-ion power batteries. *Energy Storage Mater.* **35**, 70–87 (2021).
 19. Kaboli, S. et al. Behavior of solid electrolyte in Li-polymer battery with NMC cathode via in-situ scanning electron microscopy. *Nano Lett.* **20**, 1607–1613 (2020).
 20. Wang, X. et al. Flyash/polymer composite electrolyte with internal binding interaction enables highly-stable extrinsic-interfaces of all-solid-state lithium batteries. *Chem. Eng. J.* **428**, 131041 (2022).
 21. Chen, L. et al. PEO/garnet composite electrolytes for solid-state lithium batteries: from “ceramic-in-polymer” to “polymer-in-ceramic”. *Nano Energy* **46**, 176–184 (2018).
 22. Wang, X. et al. Constructing interfacial nanolayer stabilizes 4.3 V high-voltage all-solid-state lithium batteries with PEO-based solid-state electrolyte. *Adv. Funct. Mater.* **32**, 2113068 (2022).
 23. Qiu, J. et al. Enabling stable cycling of 4.2 V high-voltage all-solid-state batteries with PEO-based solid electrolyte. *Adv. Funct. Mater.* **30**, 1909392 (2020).
 24. Yi, M. et al. Suppressing structural degradation of single crystal nickel-rich cathodes in PEO-based all-solid-state batteries: mechanistic insight and performance. *Energy Storage Mater.* **54**, 579–588 (2023).
 25. Fu, F. et al. A dual-salt PEO-based polymer electrolyte with cross-linked polymer network for high-voltage lithium metal batteries. *Chem. Eng. J.* **450**, 137776 (2022).
 26. Jeon, Y. M., Kim, S., Lee, M., Lee, W. B. & Park, J. H. Polymer-clay nanocomposite solid-state electrolyte with selective cation transport boosting and retarded lithium dendrite formation. *Adv. Energy Mater.* **10**, 2003114 (2020).
 27. Nie, K. et al. Increasing poly(ethylene oxide) stability to 4.5 V by surface coating of the cathode. *ACS Energy Lett.* **5**, 826–832 (2020).
 28. Yang, X. et al. Determining the limiting factor of the electrochemical stability window for PEO-based solid polymer electrolytes: main chain or terminal –OH group? *Energy Environ. Sci.* **13**, 1318–1325 (2020).
 29. Liu, J. et al. Nonflammable and high-voltage-tolerated polymer electrolyte achieving high stability and safety in 4.9 V-class lithium metal battery. *ACS Appl. Mater. Interfaces* **11**, 45048–45056 (2019).
 30. Xu, J. et al. Electrolyte design for Li-ion batteries under extreme operating conditions. *Nature* **614**, 694–700 (2023).
 31. Yamada, Y., Wang, J., Ko, S., Watanabe, E. & Yamada, A. Advances and issues in developing salt-concentrated battery electrolytes. *Nat. Energy* **4**, 269–280 (2019).
 32. Xiong, Z. et al. 4.2 V polymer all-solid-state lithium batteries enabled by high-concentration PEO solid electrolytes. *Energy Storage Mater.* **57**, 171–179 (2023).
 33. Wu, H. et al. A polymer-in-salt electrolyte with enhanced oxidative stability for lithium metal polymer batteries. *ACS Appl. Mater. Interfaces* **13**, 31583–31593 (2021).
 34. Efaw, C. M. et al. Localized high-concentration electrolytes get more localized through micelle-like structures. *Nat. Mater.* **22**, 1531–1539 (2023).
 35. Zhan, X. et al. Self-assembled hydrated copper coordination compounds as ionic conductors for room temperature solid-state batteries. *Nat. Commun.* **15**, 1056 (2024).
 36. Hu, J. et al. Dual fluorination of polymer electrolyte and conversion-type cathode for high-capacity all-solid-state lithium metal batteries. *Nat. Commun.* **13**, 7914 (2022).
 37. Liu, Y. et al. In situ polymerization of 1,3-dioxane as a highly compatible polymer electrolyte to enable the stable operation of 4.5 V Li-metal batteries. *Energy Environ. Sci.* **16**, 6110–6119 (2023).
 38. Xiao, P. et al. A nonflammable electrolyte for ultrahigh-voltage (4.8 V-class) Li||NCM811 cells with a wide temperature range of 100 °C. *Energy Environ. Sci.* **15**, 2435–2444 (2022).
 39. Wang, L., Wang, J. & Zuo, P. Probing battery electrochemistry with in operando synchrotron x-ray imaging techniques. *Small Methods* **2**, 1700293 (2018).
 40. Wang, L. et al. Structural distortion induced by manganese activation in a lithium-rich layered cathode. *J. Am. Chem. Soc.* **142**, 14966–14973 (2020).
 41. Zhang, F. et al. Surface regulation enables high stability of single-crystal lithium-ion cathodes at high voltage. *Nat. Commun.* **11**, 3050 (2020).
 42. Lou, S. et al. Insights into interfacial effect and local lithium-ion transport in polycrystalline cathodes of solid-state batteries. *Nat. Commun.* **11**, 5700 (2020).
 43. Liu, Q.-S. et al. Effective transport network driven by tortuosity gradient enables high-electrochem-active solid-state batteries. *Natl Sci. Rev.* **10**, nwac272 (2023).
 44. Mu, L. et al. Resolving charge distribution for compositionally heterogeneous battery cathode materials. *Nano Lett.* **22**, 1278–1286 (2022).
 45. An, H. et al. Eliminating local electrolyte failure induced by asynchronous reaction for high-loading and long-lifespan all-solid-state batteries. *Adv. Funct. Mater.* **33**, 2305186 (2023).
 46. Xu, Z. et al. Charge distribution guided by grain crystallographic orientations in polycrystalline battery materials. *Nat. Commun.* **11**, 83 (2020).
 47. Ko, D.-S. et al. Microstructural visualization of compositional changes induced by transition metal dissolution in Ni-rich layered cathode materials by high-resolution particle analysis. *Nano Energy* **56**, 434–442 (2019).
 48. Jin, Y. et al. Low-solvation electrolytes for high-voltage sodium-ion batteries. *Nat. Energy* **7**, 718–725 (2022).

49. Jeschull, F. et al. Multivalent cation transport in polymer electrolytes—reflections on an old problem. *Adv. Energy Mater.* **14**, 2302745 (2023).
50. Yagi, S. et al. A concept of dual-salt polyvalent-metal storage battery. *J. Mater. Chem. A* **2**, 1144–1149 (2014).
51. Duan, H., Li, L., Fu, X., Deng, Y. & Chen, G. A functional additive to in-situ construct stable cathode and anode interfaces for all-solid-state lithium-sulfur batteries. *Chem. Eng. J.* **450**, 138208 (2022).
52. Wang, L. et al. A strong Lewis acid imparts high ionic conductivity and interfacial stability to polymer composite electrolytes towards all-solid-state Li-metal batteries. *Sci. China Mater.* **65**, 2179–2188 (2022).
53. Andersson, R., Hernández, G. & Mindemark, J. Quantifying the ion coordination strength in polymer electrolytes. *Phys. Chem. Chem. Phys.* **24**, 16343–16352 (2022).
54. Martins, M. A. G. & Sequeira, C. A. C. Factors affecting the conductivity of divalent polymeric electrolytes. *J. Power Sources* **32**, 107–124 (1990).
55. Kosfeld, M., Westphal, B. & Kwade, A. Moisture behavior of lithium-ion battery components along the production process. *J. Energy Storage* **57**, 106174 (2023).
56. Angell, M. et al. High Coulombic efficiency aluminum-ion battery using an AlCl_3 -urea ionic liquid analog electrolyte. *Proc. Natl Acad. Sci.* **114**, 834–839 (2017).
57. Liu, T. et al. In-situ construction of a Mg-modified interface to guide uniform lithium deposition for stable all-solid-state batteries. *J. Energy Chem.* **55**, 272–278 (2021).
58. He, X. et al. Design of high-entropy tape electrolytes for compression-free solid-state batteries. *Adv. Mater.* **36**, 2307599 (2023).
59. Zhou, X. et al. Anion-reinforced solvation for a gradient inorganic-rich interphase enables high-rate and stable sodium batteries. *Angew. Chem. Int. Ed.* **61**, 5041–5048 (2022).
60. Bouchet, R. et al. Single-ion BAB triblock copolymers as highly efficient electrolytes for lithium-metal batteries. *Nat. Mater.* **12**, 452–457 (2013).
61. Li, M. et al. Ion-dipole-interaction-induced encapsulation of free residual solvent for long-cycle solid-state lithium metal batteries. *J. Am. Chem. Soc.* **145**, 25632–25642 (2023).
62. Chen, T. et al. Stable high-temperature lithium-metal batteries enabled by strong multiple ion-dipole interactions. *Angew. Chem. Int. Ed.* **61**, 7641–7647 (2022).
63. Deng, L. et al. Constructing stable anion-tuned electrode/electrolyte interphase on high-voltage $\text{Na}_3\text{V}_2(\text{PO}_4)_2\text{F}_3$ cathode for thermally-modulated fast-charging batteries. *Angew. Chem. Int. Ed.* **61**, 13411–13419 (2022).
64. Zhang, L. et al. Regulating lithium-ion transport route via adjusting lithium-ion affinity in solid polymer electrolyte. *Chem. Eng. J.* **479**, 147764 (2024).
65. Wang, X. et al. Hybrid electrolyte with dual-anion-aggregated solvation sheath for stabilizing high-voltage lithium-metal batteries. *Adv. Mater.* **33**, 2007945 (2021).
66. Zhang, J. et al. Interfacial design for a 4.6 V high-voltage single-crystalline LiCoO_2 cathode. *Adv. Mater.* **34**, 2108353 (2022).
67. Li, L. et al. Highly fluorinated Al-centered lithium salt boosting the interfacial compatibility of Li-metal batteries. *ACS Energy Lett.* **7**, 591–598 (2022).
68. Han, S., Li, Z., Zhang, Y., Lei, D. & Wang, C. In-situ formation of a nanoscale lithium aluminum alloy in lithium metal for high-load battery anode. *Energy Storage Mater.* **48**, 384–392 (2022).
69. Li Y., Bai F., Li C., Wang Y., Li T. Understanding the inorganic-rich feature of anion-derived solid electrolyte interphase. *Adv. Energy Mater.* **14**, 2304414 (2024).
70. Yang, M. et al. Roll-to-roll fabricated polymer composites filled with subnanosheets exhibiting high energy density and cyclic stability at 200 °C. *Nat. Energy* **9**, 143–153 (2024).
71. Lu, Y., Tu, Z. & Archer, L. A. Stable lithium electrodeposition in liquid and nanoporous solid electrolytes. *Nat. Mater.* **13**, 961–969 (2014).
72. Li, S. et al. Mutual modulation between surface chemistry and bulk microstructure within secondary particles of nickel-rich layered oxides. *Nat. Commun.* **11**, 4433 (2020).
73. Jiang, J. et al. Construction of lithophilic solid electrolyte interfaces with a bottom-up nucleation barrier difference for low-N/P ratio Li-metal batteries. *Energy Storage Mater.* **54**, 885–894 (2023).
74. Wu, M., Wen, Z., Jin, J. & Cui, Y. Effects of combinatorial AlCl_3 and pyrrole on the SEI formation and electrochemical performance of Li electrode. *Electrochim. Acta* **103**, 199–205 (2013).
75. Miao, X. et al. AlF_3 -modified anode-electrolyte interface for effective Na dendrites restriction in NASICON-based solid-state electrolyte. *Energy Storage Mater.* **30**, 170–178 (2020).
76. Liu, Q. et al. Fast lithium transport kinetics regulated by low energy-barrier Li_xMnO_2 for long-life lithium metal batteries. *Energy Storage Mater.* **41**, 1–7 (2021).
77. Kresse, G. & Furthmüller, J. Efficiency of ab-initio total energy calculations for metals and semiconductors using a plane-wave basis set. *Comput. Mater. Sci.* **6**, 15–50 (1996).
78. Perdew, J. P., Burke, K. & Ernzerhof, M. Generalized gradient approximation made simple. *Phys. Rev. Lett.* **77**, 3865–3868 (1996).
79. Blöchl PEJPrB, condensed matter. Projector augmented-wave method. *Phys. Rev. B, Condens. Matter* **50**, 17953–17979 (1994).
80. Grimme, S. Semiempirical GGA-type density functional constructed with a long-range dispersion correction. *J. Comput. Chem.* **27**, 1787–1799 (2006).
81. Jorgensen, W. L., Maxwell, D. S. & Tirado-Rives, J. Development and testing of the OPLS all-atom force field on conformational energetics and properties of organic liquids. *J. Am. Chem. Soc.* **118**, 11225–11236 (1996).
82. Jeon, J., Lee, H., Choi, J.-H. & Cho, M. Modeling and simulation of concentrated aqueous solutions of LiTFSI for battery applications. *J. Phys. Chem. C* **124**, 11790–11799 (2020).
83. Manna, S. S. & Pathak, B. Screening of ionic liquid-based electrolytes for Al dual-ion batteries: thermodynamic cycle and combined MD-DFT approaches. *J. Phys. Chem. C* **127**, 8913–8924 (2023).
84. Zhang, Y. et al. Modelling electrified microporous carbon/electrolyte electrochemical interface and unraveling charge storage mechanism by machine learning accelerated molecular dynamics. *Energy Storage Mater.* **63**, 103069 (2023).
85. Wang, F. & Cheng, J. Understanding the solvation structures of glyme-based electrolytes by machine learning molecular dynamics. *Chin. J. Struct. Chem.* **42**, 100061 (2023).
86. Thompson, A. P., Swiler, L. P., Trott, C. R., Foiles, S. M. & Tucker, G. J. Spectral neighbor analysis method for automated generation of quantum-accurate interatomic potentials. *J. Comput. Phys.* **285**, 316–330 (2015).
87. Yao, N., Chen, X., Fu, Z.-H. & Zhang, Q. Applying classical, ab initio, and machine-learning molecular dynamics simulations to the liquid electrolyte for rechargeable batteries. *Chem. Rev.* **122**, 10970–11021 (2022).
88. Hu, T. et al. Impact of the local environment on Li ion transport in inorganic components of solid electrolyte interphases. *J. Am. Chem. Soc.* **145**, 1327–1333 (2022).
89. Wu, Z. et al. Deciphering and modulating energetics of solvation structure enables aggressive high-voltage chemistry of Li metal batteries. *Chem.* **9**, 650–664 (2023).

Acknowledgements

This work was supported by the Opening Project of State Key Laboratory of Space Power-Sources, the National Natural Science Foundation of China (Nos. 22075063, U1932205, 22279026, 92372110), the Chinesisch-Deutsches Mobilitätsprogramm (M-0281), the Fundamental Research Funds for the Central Universities (Grant No. HIT.OCEF.2023039, No.HIT OCEF.2022017), Natural Science Funds of Heilongjiang Province (Nos.

ZD2019B001, YQ2021B003), the Heilongjiang Touyan Team (No. HITY-20190033), the Natural Science Fund for Distinguished Young Scholars of Chongqing (cstc2021jcyj-jqX0003), the “Young Scientist Studio” of Harbin Institute of Technology (HIT), and funds from Chongqing Research Institute of HIT. We thank the beamline BL13HB, BL18B, and BLO8U1A at Shanghai Synchrotron Radiation Facility (SSRF) for STXM measurements and SR-CT measurements.

Author contributions

All authors have given approval to the final version of the manuscript. Jiajun Wang proposed the research direction, conceived, and led the project. Hanwen An designed and performed the experiments, and drafted the manuscript. Menglu Li, Qingsong Liu, Jiaxuan Liu, and Yajie Song performed the STXM and CT experiments, analyzed and discussed the experimental results and drafted the manuscript. Biao Deng provided synchrotron radiation experiment conditions in SSRF. Zhihang Yu, Xingjiang Liu provided the experimental conditions for pouch cells. All authors participated in discussions and gave valuable suggestions.

Competing interests

The authors declare no competing interests.

Additional information

Supplementary information The online version contains supplementary material available at <https://doi.org/10.1038/s41467-024-53094-8>.

Correspondence and requests for materials should be addressed to Xingjiang Liu or Jiajun Wang.

Peer review information *Nature Communications* thanks Michel Armand, Hyung-Seok Lim and the other, anonymous, reviewer for their contribution to the peer review of this work. A peer review file is available.

Reprints and permissions information is available at <http://www.nature.com/reprints>

Publisher’s note Springer Nature remains neutral with regard to jurisdictional claims in published maps and institutional affiliations.

Open Access This article is licensed under a Creative Commons Attribution-NonCommercial-NoDerivatives 4.0 International License, which permits any non-commercial use, sharing, distribution and reproduction in any medium or format, as long as you give appropriate credit to the original author(s) and the source, provide a link to the Creative Commons licence, and indicate if you modified the licensed material. You do not have permission under this licence to share adapted material derived from this article or parts of it. The images or other third party material in this article are included in the article’s Creative Commons licence, unless indicated otherwise in a credit line to the material. If material is not included in the article’s Creative Commons licence and your intended use is not permitted by statutory regulation or exceeds the permitted use, you will need to obtain permission directly from the copyright holder. To view a copy of this licence, visit <http://creativecommons.org/licenses/by-nc-nd/4.0/>.

© The Author(s) 2024